

Search for Trilinear Neutral Gauge Boson Couplings in $Z\gamma$ production at $\sqrt{s} = 189$ GeV at LEP

The OPAL Collaboration

Abstract

The data recorded at a centre-of-mass energy of 189 GeV by the OPAL detector at LEP are used to search for trilinear couplings of the neutral gauge bosons in the process $e^+e^- \rightarrow Z\gamma$. The cross-sections for multihadronic events with an energetic isolated photon, and for events with a high energy photon accompanied by missing energy are measured. These cross-sections and the photon energy, polar angle and isolation angle distributions are compared to the Standard Model predictions and to the theoretical expectations of a model allowing for $Z\gamma Z$ and $Z\gamma\gamma$ vertices. Since no significant deviations with respect to the Standard Model expectations are found, constraints are derived on the strength of neutral trilinear gauge couplings.

(Submitted to Eur. Phys. J.)

The OPAL Collaboration

G. Abbiendi², K. Ackerstaff⁸, C. Ainsley⁵, P.F. Akesson³, G. Alexander²², J. Allison¹⁶,
 K.J. Anderson⁹, S. Arcelli¹⁷, S. Asai²³, S.F. Ashby¹, D. Axen²⁷, G. Azuelos^{18,a}, I. Bailey²⁶, A.H. Ball⁸,
 E. Barberio⁸, R.J. Barlow¹⁶, J.R. Batley⁵, S. Baumann³, T. Behnke²⁵, K.W. Bell²⁰, G. Bella²²,
 A. Bellerive⁹, S. Bentvelsen⁸, S. Bethke^{14,i}, O. Biebel^{14,i}, I.J. Bloodworth¹, P. Bock¹¹, J. Böhme^{14,h},
 O. Boeriu¹⁰, D. Bonacorsi², M. Boutemour³¹, S. Braibant⁸, P. Bright-Thomas¹, L. Brigliadori²,
 R.M. Brown²⁰, H.J. Burckhart⁸, J. Cammin³, P. Capiluppi², R.K. Carnegie⁶, A.A. Carter¹³,
 J.R. Carter⁵, C.Y. Chang¹⁷, D.G. Charlton^{1,b}, C. Ciocca², P.E.L. Clarke¹⁵, E. Clay¹⁵, I. Cohen²²,
 O.C. Cooke⁸, J. Couchman¹⁵, C. Couyoumtzelis¹³, R.L. Coxe⁹, M. Cuffiani², S. Dado²¹,
 G.M. Dallavalle², S. Dallison¹⁶, A. de Roeck⁸, P. Dervan¹⁵, K. Desch²⁵, B. Dienes^{30,h}, M.S. Dixit⁷,
 M. Donkers⁶, J. Dubbert³¹, E. Duchovni²⁴, G. Duckeck³¹, I.P. Duerdoth¹⁶, P.G. Estabrooks⁶,
 E. Etzion²², F. Fabbri², M. Fanti², L. Feld¹⁰, P. Ferrari¹², F. Fiedler⁸, I. Fleck¹⁰, M. Ford⁵, A. Frey⁸,
 A. Fürtjes⁸, D.I. Futyan¹⁶, P. Gagnon¹², J.W. Gary⁴, G. Gaycken²⁵, C. Geich-Gimbel³, G. Giacomelli²,
 P. Giacomelli⁸, D. Glenzinski⁹, J. Goldberg²¹, C. Grandi², K. Graham²⁶, E. Gross²⁴, J. Grunhaus²²,
 M. Gruwé²⁵, P.O. Günther³, C. Hajdu²⁹, G.G. Hanson¹², M. Hansroul⁸, M. Hapke¹³, K. Harder²⁵,
 A. Harel²¹, C.K. Hargrove⁷, M. Harin-Dirac⁴, A. Hauke³, M. Hauschild⁸, C.M. Hawkes¹,
 R. Hawkings²⁵, R.J. Hemingway⁶, C. Hensel²⁵, G. Herten¹⁰, R.D. Heuer²⁵, M.D. Hildreth⁸, J.C. Hill⁵,
 A. Hocker⁹, K. Hoffman⁸, R.J. Homer¹, A.K. Honma⁸, D. Horváth^{29,c}, K.R. Hossain²⁸, R. Howard²⁷,
 P. Hüntemeyer²⁵, P. Igo-Kemenes¹¹, K. Ishii²³, F.R. Jacob²⁰, A. Jawahery¹⁷, H. Jeremie¹⁸,
 C.R. Jones⁵, P. Jovanovic¹, T.R. Junk⁶, N. Kanaya²³, J. Kanzaki²³, G. Karapetian¹⁸, D. Karlen⁶,
 V. Kartvelishvili¹⁶, K. Kawagoe²³, T. Kawamoto²³, R.K. Keeler²⁶, R.G. Kellogg¹⁷, B.W. Kennedy²⁰,
 D.H. Kim¹⁹, K. Klein¹¹, A. Klier²⁴, T. Kobayashi²³, M. Kobel³, T.P. Kokott³, S. Komamiya²³,
 R.V. Kowalewski²⁶, T. Kress⁴, P. Krieger⁶, J. von Krogh¹¹, T. Kuhl³, M. Kupper²⁴, P. Kyberd¹³,
 G.D. Lafferty¹⁶, H. Landsman²¹, D. Lanske¹⁴, I. Lawson²⁶, J.G. Layter⁴, A. Leins³¹, D. Lellouch²⁴,
 J. Letts¹², L. Levinson²⁴, R. Liebisch¹¹, J. Lillich¹⁰, B. List⁸, C. Littlewood⁵, A.W. Lloyd¹,
 S.L. Lloyd¹³, F.K. Loebinger¹⁶, G.D. Long²⁶, M.J. Losty⁷, J. Lu²⁷, J. Ludwig¹⁰, A. Macchiolo¹⁸,
 A. Macpherson²⁸, W. Mader³, M. Mannelli⁸, S. Marcellini², T.E. Marchant¹⁶, A.J. Martin¹³,
 J.P. Martin¹⁸, G. Martinez¹⁷, T. Mashimo²³, P. Mättig²⁴, W.J. McDonald²⁸, J. McKenna²⁷,
 T.J. McMahon¹, R.A. McPherson²⁶, F. Meijers⁸, P. Mendez-Lorenzo³¹, F.S. Merritt⁹, H. Mes⁷,
 A. Michelini², S. Mihara²³, G. Mikenberg²⁴, D.J. Miller¹⁵, W. Mohr¹⁰, A. Montanari², T. Mori²³,
 K. Nagai⁸, I. Nakamura²³, H.A. Neal^{12,f}, R. Nisius⁸, S.W. O’Neale¹, F.G. Oakham⁷, F. Odorici²,
 H.O. Ogren¹², A. Oh⁸, A. Okpara¹¹, M.J. Oreglia⁹, S. Orito²³, G. Pásztor^{8,j}, J.R. Pater¹⁶,
 G.N. Patrick²⁰, J. Patt¹⁰, P. Pfeifenschneider¹⁴, J.E. Pilcher⁹, J. Pinfold²⁸, D.E. Plane⁸, B. Poli²,
 J. Polok⁸, O. Pooth⁸, M. Przybycień^{8,d}, A. Quadt⁸, C. Rembser⁸, H. Rick⁴, S.A. Robins²¹,
 N. Rodning²⁸, J.M. Roney²⁶, S. Rosati³, K. Roscoe¹⁶, A.M. Rossi², Y. Rozen²¹, K. Runge¹⁰,
 O. Runolfsson⁸, D.R. Rust¹², K. Sachs⁶, T. Saeki²³, O. Sahr³¹, E.K.G. Sarkisyan²², C. Sbarra²⁶,
 A.D. Schaile³¹, O. Schaile³¹, P. Scharff-Hansen⁸, S. Schmitt¹¹, M. Schröder⁸, M. Schumacher²⁵,
 C. Schwick⁸, W.G. Scott²⁰, R. Seuster^{14,h}, T.G. Shears⁸, B.C. Shen⁴, C.H. Shepherd-Themistocleous⁵,
 P. Sherwood¹⁵, G.P. Siroli², A. Skuja¹⁷, A.M. Smith⁸, G.A. Snow¹⁷, R. Sobie²⁶,
 S. Söldner-Rembold^{10,e}, S. Spagnolo²⁰, M. Sproston²⁰, A. Stahl³, K. Stephens¹⁶, K. Stoll¹⁰, D. Strom¹⁹,
 R. Ströhmer³¹, B. Surrow⁸, S.D. Talbot¹, S. Tarem²¹, R.J. Taylor¹⁵, R. Teuscher⁹, M. Thiergen¹⁰,
 J. Thomas¹⁵, M.A. Thomson⁸, E. Torrence⁹, S. Towers⁶, T. Trefzger³¹, I. Trigger⁸, Z. Trócsányi^{30,g},
 E. Tsur²², M.F. Turner-Watson¹, I. Ueda²³, P. Vannerem¹⁰, M. Verzocchi⁸, H. Voss⁸, J. Vosseveld⁸,
 D. Waller⁶, C.P. Ward⁵, D.R. Ward⁵, P.M. Watkins¹, A.T. Watson¹, N.K. Watson¹, P.S. Wells⁸,
 T. Wengler⁸, N. Wormes³, D. Wetterling¹¹, J.S. White⁶, G.W. Wilson¹⁶, J.A. Wilson¹, T.R. Wyatt¹⁶,
 S. Yamashita²³, V. Zacek¹⁸, D. Zer-Zion⁸

- ¹School of Physics and Astronomy, University of Birmingham, Birmingham B15 2TT, UK
- ²Dipartimento di Fisica dell' Università di Bologna and INFN, I-40126 Bologna, Italy
- ³Physikalisches Institut, Universität Bonn, D-53115 Bonn, Germany
- ⁴Department of Physics, University of California, Riverside CA 92521, USA
- ⁵Cavendish Laboratory, Cambridge CB3 0HE, UK
- ⁶Ottawa-Carleton Institute for Physics, Department of Physics, Carleton University, Ottawa, Ontario K1S 5B6, Canada
- ⁷Centre for Research in Particle Physics, Carleton University, Ottawa, Ontario K1S 5B6, Canada
- ⁸CERN, European Organisation for Nuclear Research, CH-1211 Geneva 23, Switzerland
- ⁹Enrico Fermi Institute and Department of Physics, University of Chicago, Chicago IL 60637, USA
- ¹⁰Fakultät für Physik, Albert Ludwigs Universität, D-79104 Freiburg, Germany
- ¹¹Physikalisches Institut, Universität Heidelberg, D-69120 Heidelberg, Germany
- ¹²Indiana University, Department of Physics, Swain Hall West 117, Bloomington IN 47405, USA
- ¹³Queen Mary and Westfield College, University of London, London E1 4NS, UK
- ¹⁴Technische Hochschule Aachen, III Physikalisches Institut, Sommerfeldstrasse 26-28, D-52056 Aachen, Germany
- ¹⁵University College London, London WC1E 6BT, UK
- ¹⁶Department of Physics, Schuster Laboratory, The University, Manchester M13 9PL, UK
- ¹⁷Department of Physics, University of Maryland, College Park, MD 20742, USA
- ¹⁸Laboratoire de Physique Nucléaire, Université de Montréal, Montréal, Quebec H3C 3J7, Canada
- ¹⁹University of Oregon, Department of Physics, Eugene OR 97403, USA
- ²⁰CLRC Rutherford Appleton Laboratory, Chilton, Didcot, Oxfordshire OX11 0QX, UK
- ²¹Department of Physics, Technion-Israel Institute of Technology, Haifa 32000, Israel
- ²²Department of Physics and Astronomy, Tel Aviv University, Tel Aviv 69978, Israel
- ²³International Centre for Elementary Particle Physics and Department of Physics, University of Tokyo, Tokyo 113-0033, and Kobe University, Kobe 657-8501, Japan
- ²⁴Particle Physics Department, Weizmann Institute of Science, Rehovot 76100, Israel
- ²⁵Universität Hamburg/DESY, II Institut für Experimental Physik, Notkestrasse 85, D-22607 Hamburg, Germany
- ²⁶University of Victoria, Department of Physics, P O Box 3055, Victoria BC V8W 3P6, Canada
- ²⁷University of British Columbia, Department of Physics, Vancouver BC V6T 1Z1, Canada
- ²⁸University of Alberta, Department of Physics, Edmonton AB T6G 2J1, Canada
- ²⁹Research Institute for Particle and Nuclear Physics, H-1525 Budapest, P O Box 49, Hungary
- ³⁰Institute of Nuclear Research, H-4001 Debrecen, P O Box 51, Hungary
- ³¹Ludwigs-Maximilians-Universität München, Sektion Physik, Am Coulombwall 1, D-85748 Garching, Germany

^a and at TRIUMF, Vancouver, Canada V6T 2A3

^b and Royal Society University Research Fellow

^c and Institute of Nuclear Research, Debrecen, Hungary

^d and University of Mining and Metallurgy, Cracow

^e and Heisenberg Fellow

^f now at Yale University, Dept of Physics, New Haven, USA

^g and Department of Experimental Physics, Lajos Kossuth University, Debrecen, Hungary

^h and MPI München

ⁱ now at MPI für Physik, 80805 München

^j and Research Institute for Particle and Nuclear Physics, Budapest, Hungary.

1 Introduction

The self-interactions of the gauge bosons are consequences of the non-Abelian structure of the electroweak sector of the Standard Model; therefore, the strength of trilinear and quartic gauge couplings is predicted as a result of the gauge symmetry of the theory. The study of trilinear gauge boson couplings in two-boson production processes is within the reach of existing accelerators and measurements of WWZ and WW γ couplings are being performed with increasing precision in e^+e^- [1] and $p\bar{p}$ [2] collisions. While non-zero values are predicted for the couplings in the triple and quartic vertices involving charged gauge bosons, the tree level vertices $Z\gamma Z$, $Z\gamma\gamma$ and ZZZ are not generated by the Standard Model Lagrangian; higher order corrections through virtual loops contribute at the level of 10^{-4} [3], well below the current experimental sensitivity. Nevertheless, new phenomena with a characteristic mass scale above the present experimental threshold might lead to tree-level neutral trilinear gauge couplings (NTGC) in the effective Lagrangian [4,5] parametrising the residual low energy effects from new physics. For example, as suggested in [6], virtual effects from new heavy fermions having non-standard couplings to the gauge bosons might generate sizeable anomalous contributions.

The most general $Z\gamma V$ vertex (where V is the intermediate virtual boson, either photon or a Z) compatible with Lorentz invariance and electro-magnetic gauge invariance involves four independent operators, corresponding to the allowed helicity states for the $Z\gamma$ pair [7,8]. Therefore, in a model independent description, there exist eight couplings: four of them (h_i^Z , $i = 1, \dots, 4$) corresponding to $V=Z$ and four (h_i^γ) corresponding to $V=\gamma$. The vertex function was first given in [8]. In this analysis, we adopt the most recent convention established in [6]. The lowest dimensional operators associated to the $h_i^{Z,\gamma}$ ($i = 1, 3$) couplings are of dimension six, while dimension eight operators are associated to $h_i^{Z,\gamma}$ ($i = 2, 4$). As discussed in [6], no additional symmetry constraints, such as the $SU(2)\times U(1)$ gauge invariance usually assumed in the case of WWV anomalous couplings [9], can help in reducing the number of free parameters in the neutral gauge vertex, since operators of even higher dimensionality would be required. Therefore a model independent approach is used which retains all eight couplings.

In this paper, the process $e^+e^- \rightarrow Z\gamma$ at $\sqrt{s} = 189$ GeV is investigated through the final states $q\bar{q}\gamma$ and $\nu\bar{\nu}\gamma$, the dominant decay modes of the Z boson, with the aim of searching for $Z\gamma Z$ and $Z\gamma\gamma$ couplings. Experimental constraints on these couplings have been produced in the past from the analysis of LEP data at lower energies [10] and of the TEVATRON data [11]. The analysis presented here has higher sensitivity due to the increased centre-of-mass energy and due to the large data sample collected during the 1998 operation of LEP. It also benefits from the recent clarification [6] of the theoretical framework in which neutral gauge boson self-interactions can be described. A recent analysis based on data collected at $\sqrt{s} = 189$ GeV by the L3 collaboration [12] adopts the same convention as in this paper. On the other hand, due to this different convention, the comparison of the results presented here and in [12] with previous published results is not straightforward.

In e^+e^- collisions, the production of $Z\gamma$ final states via anomalous neutral gauge couplings has a large irreducible Standard Model background from Z^0 production with hard initial state radiation (ISR). Small contributions to $q\bar{q}\gamma$ production also arise from $e^+e^- \rightarrow \gamma\gamma^* \rightarrow \gamma q\bar{q}$ and from final state radiation in $q\bar{q}$ production. In the $\nu\bar{\nu}\gamma$ channel, final states arising from the exchange of a W boson in the t -channel also contribute to the cross-section, although their contribution is small within the $Z\gamma$ signal acceptance used in this analysis. As a general property, the Z and γ produced at the anomalous vertices are more isotropically distributed than the dominant Standard Model background, which is characterized by the strongly forward peaked angular distribution of initial state radiation. Therefore, deviations from the Standard Model predictions due to $Z\gamma V$ couplings would be more pronounced for large angles between the beam direction and the photon. In the $q\bar{q}\gamma$ final state, the angular distribution of the jets can also be exploited in order to gain sensitivity to anomalous couplings, due

to the resulting enhancement of the longitudinal polarisation of the Z boson affecting the fermion decay angle. On the other hand, the photon energy spectrum has a marginal sensitivity, due to the kinematic constraints from the fixed centre-of-mass energy and the narrow Z resonance. Since all the terms in the $Z\gamma V$ vertex are proportional to the momenta of the gauge bosons involved, this results in an enhancement of the sensitivity to NTGC as the centre-of-mass energy increases. Finally, the experimental signature of the anomalous $h_i^{Z,\gamma}$ couplings depends on the CP parity of the associated operators. The vertex terms proportional to $h_1^{Z,\gamma}$ and $h_2^{Z,\gamma}$ violate CP and, hence, do not interfere with the CP conserving Standard Model amplitudes. As a result the total and differential cross-sections receive only additive contributions from the anomalous processes. The remaining couplings, associated to CP even terms, lead to amplitudes which interfere with the Standard Model; therefore the differential and total cross-sections are enhanced or suppressed depending on the sign and the size of the $h_i^{Z,\gamma}$ ($i = 3, 4$) couplings.

2 Detector and Monte Carlo Simulation

The OPAL detector, described in detail in [13], consists of a central tracking system inside a solenoid providing a magnetic field of 0.435 T, and of an electromagnetic calorimeter, complemented by a presampling system and an array of scintillation counters for time-of-flight measurements; hadron calorimetry is obtained by instrumenting the magnet return yoke which is surrounded by muon chambers. A system of forward calorimeters extends the angular coverage of the detector down to a polar angle¹ of 24 mrad. However, due to the installation in 1996 of a thick tungsten shield designed to protect the tracking chambers from synchrotron radiation background, the effective limit of electromagnetic hermeticity is around 33 mrad. The integrated luminosity of the data samples is determined from the rate of small angle Bhabha scattering events observed in the silicon-tungsten calorimeter [14] with a precision of 0.22%.

Track reconstruction is performed by combining the information from a silicon microvertex detector, a vertex drift chamber, a large volume jet drift chamber and an outer layer of drift chambers for the measurement of the z coordinate. The most relevant subdetector for the event topologies used in the analysis presented here is the electromagnetic calorimeter. It consists of an array of 9440 lead-glass blocks in the barrel ($|\cos\theta| < 0.82$) arranged in an almost-pointing geometry and two dome-shaped end caps, each of 1132 longitudinally aligned lead-glass blocks, covering the polar angle range $0.81 < |\cos\theta| < 0.984$. Trigger signals [15], based on energy deposits in the lead-glass blocks and also on a coincidence of energy in the barrel electromagnetic calorimeter and a hit in the time-of-flight system, guarantee full trigger efficiency for both the $q\bar{q}\gamma$ and the $\nu\bar{\nu}\gamma$ events falling within the signal definition criteria used in this analysis.

The Standard Model processes leading to the $q\bar{q}\gamma$ and $\nu\bar{\nu}\gamma$ final states have been simulated using the Monte Carlo generators KK2f [16] for the hadronic channel and KORALZ [17] and NUNUGPV98 [18] for the missing energy channel. For the $q\bar{q}\gamma$ channel, the fragmentation, which includes photon radiation from the quarks, and the hadronization are simulated with the JETSET package [19] tuned on the basis of extensive studies of hadronic events at the Z resonance as described in [20]. The grc4f [21] generator has been used to estimate the background to the $q\bar{q}\gamma$ channel from four-fermion production. The contribution to the background from two-photon interactions has been studied with the Monte Carlo generators PHOJET [22], for the untagged and double-tagged events, and HERWIG [23], for the single-tagged events and charged current deep inelastic scattering events. In the $\nu\bar{\nu}\gamma$ channel,

¹In the OPAL coordinate system, θ is the polar angle defined with respect to the electron beam direction and ϕ is the azimuthal angle.

the contamination from Bhabha events has been estimated using the BHWIDE [24] and TEEGG [25] generators. The contamination from four-fermion production has been studied using grc4f [21] and KORALW [26], while to determine the background from two-photon interactions the VERMASEREN [27] Monte Carlo generator has been used. The RADCOR [28] Monte Carlo has been used to study the $e^+e^- \rightarrow \gamma\gamma$ background and the energy response of the calorimeter to photons. All the Monte Carlo samples described above were processed through the OPAL detector simulation [29]. For the interpretation of the data, as will be described in more detail in section 4, a Monte Carlo generator [30], based on the matrix element for $f\bar{f}\gamma$ production in e^+e^- collisions and including the contributions from NTGC, has been used.

3 Event Selection and Cross-Section Measurements

3.1 The selection of $q\bar{q}\gamma$ events

The selection of hadronic events with isolated high energy photons is performed on events preselected as high multiplicity hadronic events in a data sample corresponding to an integrated luminosity of 176.2 pb^{-1} with an average centre-of-mass energy of 188.6 GeV. The preselection criteria, described in [31], are based on the track and cluster multiplicity, on the visible energy and on the longitudinal imbalance of the energy measured in the electromagnetic calorimeter. The events satisfying the preselection requirements are processed by a photon search algorithm.

The photon identification is based on an algorithm optimised for photon search in hadronic events described in [32]. Electromagnetic clusters without associated tracks in the central detector are accepted as photon candidates if their energy is higher than 5% of the beam energy and their polar angle lies in the acceptance region of the lead-glass calorimeter. The number of lead-glass blocks involved and the energy sharing among them are required to correspond to typical patterns defined for photon identification in the OPAL calorimeter. An isolation criterion is then applied in order to reject electromagnetic clusters associated with jets. The total energy deposition in the electromagnetic calorimeter (not associated to the photon candidate) within a cone of 15° around the photon flight direction is required to be less than 2 GeV. In addition, the sum of the momenta of tracks which, extrapolated to the calorimeter surface, fall inside a 15° cone around the photon impact point is also required to be lower than 2 GeV. Finally, systems of one or two well reconstructed tracks associated with electromagnetic clusters, consistent with a photon conversion according to the criteria described in [33], are included if the reconstructed photon satisfies the criteria listed above. The photon identification algorithm has been extensively studied in order to assess the level of accuracy of the estimate of the efficiency obtained from Monte Carlo $q\bar{q}\gamma$ events. In particular, the selection criteria of the algorithm have been adjusted in order to minimise their sensitivity to unsatisfactory modelling in the simulation. A residual discrepancy in the identification efficiency for converted photons has been observed and taken into account as a correction of 1.25% to the overall selection efficiency. As an example of the quality of the modelling of the photon identification algorithm, figure 1 shows the angle between the photon candidate and the closest track in the event and the total charged energy in the isolation cone.

After the photon search, all the clusters and tracks in the event which are not associated to the most energetic photon candidate are grouped into jets according to the Durham k_T [34] scheme with resolution parameter $y = 0.02$. If more than four jets are reconstructed, the event is forced to have four jets in addition to the isolated high energy photon.

In $e^+e^- \rightarrow Z\gamma$ at $\sqrt{s} = 189 \text{ GeV}$ the photon energy spectrum is peaked at approximately 72 GeV, reflecting the sharp Z resonance. In order to select the topology corresponding to a high energy photon

recoiling against a hadronic system of invariant mass equal to the Z boson mass, the signal definition is based on kinematic cuts applied to the most energetic photon in the event:

$$50 \text{ GeV} < E_\gamma < 90 \text{ GeV} ;$$

$$15^\circ < \theta_\gamma < 165^\circ ,$$

where E_γ and θ_γ are the photon energy and polar angle, respectively.

To improve the photon energy resolution and suppress further the background from non- $q\bar{q}\gamma$ events and the feedthrough from events outside the signal definition, a kinematic fit is applied to all the events with at least one photon of energy larger than 30 GeV. The fit [31] imposes energy and momentum conservation using as input the photon and the jet momenta. Undetected ISR is allowed to compensate for missing longitudinal momentum in the beam pipe region if the χ^2 probability of the fit is smaller than 1%.

From a study of Monte Carlo $q\bar{q}\gamma$ events, the kinematic fit improves the photon energy resolution by a factor two. The events for which the fit converges (99.5%) are finally selected if the fitted values of E_γ and θ_γ satisfy the signal definition cuts. In order to suppress contamination from photons originating from the jets, only the sub-sample in which $\alpha_{\gamma\text{-jet}} > 30^\circ$, where $\alpha_{\gamma\text{-jet}}$ is the angle between the photon and the closest jet, is retained for the analysis.

The selection efficiency and the feedthrough in the kinematic acceptance are listed in table 1. They have been estimated from fully simulated $e^+e^- \rightarrow q\bar{q}$ Monte Carlo events, where the signal-like topology arises from radiative return to the Z resonance. The efficiency has been calculated with respect to the kinematic signal acceptance defined above. The feedthrough represents the fraction of selected events which do not belong to the kinematic acceptance; it is mainly due to resolution effects, but it includes also a small contamination (0.35%) due to non-ISR photon candidates in $e^+e^- \rightarrow q\bar{q}$ events falling in the signal acceptance after reconstruction. Both the efficiency and the feedthrough are corrected for the aforementioned residual disagreement between the performance of the photon search algorithm in the data and in the Monte Carlo.

The numbers of events selected in the data and in the Monte Carlo samples are listed in table 2. Figure 2 shows the distributions of the photon energy and polar angle and angular separation with respect to the closest jet for the events selected in the data, compared with the Standard Model expectation from Monte Carlo. The total background (2.5% of the selected events) comes from four-fermion production (1.59%) two-photon interactions (0.59%) and tau-pair production (0.34%). The agreement between the data and the Monte Carlo is in general satisfactory, except perhaps in the photon energy distribution where a slight deficit of events is observed in the radiative return peak.

3.2 The selection of $\nu\bar{\nu}\gamma$ events

The selection of events with an isolated high energy photon accompanied by missing energy and low activity in the detector follows the single-photon analysis described in [35]. The data sample used in the analysis corresponds to an integrated luminosity of 177.3 pb^{-1} , with an average centre-of-mass energy of 188.6 GeV. After the single photon selection, 643 events are retained in the data. The same additional conditions which define the kinematic acceptance in the $q\bar{q}\gamma$ channel, $50 \text{ GeV} < E_\gamma < 90 \text{ GeV}$ and $15^\circ < \theta_\gamma < 165^\circ$, are then applied to the most energetic photon in the electromagnetic calorimeter.

The predicted efficiency and the feedthrough in the kinematic acceptance are listed in table 1. They have been estimated averaging the predictions of the KORALZ and the NUNUGPV98 Monte Carlo, which in the signal acceptance agree within $(0.2\pm 0.5)\%$ in the efficiency and $(1\pm 9)\%$ in the feedthrough.

The number of events selected in the data are listed in table 3, together with those expected from all the relevant physics processes and from instrumental backgrounds. As potential sources of physics background, four-fermion processes, radiative Bhabha and $e^+e^- \rightarrow \gamma\gamma$ events have been considered, while the residual cosmic ray and beam-related contamination have been estimated using control samples enriched in these backgrounds. Both these sources result in an overall negligible (0.24%) contribution to the selected events. Figure 3 shows the distributions of the energy and of the polar angle of the photon for the selected events, compared with the Standard Model expectation.

3.3 Cross-section Measurements

From the number of observed events in each channel and from the predicted efficiency, feedthrough and backgrounds, as presented in sections 3.1 and 3.2, the cross-sections within the kinematic signal acceptance are measured to be:

$$\begin{aligned}\sigma_{q\bar{q}\gamma} &= 9.42 \pm 0.25 \text{ (stat.)} \pm 0.15 \text{ (syst.) pb} \\ \sigma_{\nu\bar{\nu}\gamma} &= 2.52 \pm 0.13 \text{ (stat.)} \pm 0.05 \text{ (syst.) pb.}\end{aligned}$$

These measurements are in reasonable agreement, within the errors which are dominated by the statistical uncertainty, with the predictions from the Standard Model, which are respectively $\sigma_{q\bar{q}\gamma}^{\text{SM}} = 9.75 \pm 0.03 \text{ pb}$ and $\sigma_{\nu\bar{\nu}\gamma}^{\text{SM}} = 2.81 \pm 0.02 \text{ pb}$. The predicted $q\bar{q}\gamma$ cross-section is obtained from KK2f, while the $\nu\bar{\nu}\gamma$ cross-section is the average of the predictions of KORALZ and NUNUGPV98 which are consistent within $(1.6 \pm 1.1)\%$. The errors associated with the Standard Model predictions come from the Monte Carlo statistics. Taking into account the experimental systematic uncertainties discussed in the following section, the overall discrepancy corresponds to -1.1 standard deviations for the $q\bar{q}\gamma$ channel and -2.1 for the $\nu\bar{\nu}\gamma$ channel.

3.4 Systematic Errors

The different sources of systematic uncertainties affecting the cross-section measurements are summarised in table 4 and are discussed in the following:

Systematics specific to the $q\bar{q}\gamma$ channel:

- The uncertainty on the selection efficiency. Contributions to this uncertainty come from imperfect modelling of the material in the detector, affecting the estimate of the photon conversion rate (0.77%) , from inaccuracies in the modelling of the identification efficiency for converted photons (0.62%) , from uncertainty in the simulation of the track-cluster association at forward angles (0.64%) and from the photon isolation criterion (0.26%) . The total uncertainty coming from the modelling of the selection efficiency translates into a relative error on the cross-section of 1.2% . The uncertainties arising from limited Monte Carlo statistics used to evaluate the efficiency and the feedthrough are respectively 0.14% and 0.07% .

- The modelling of the jet reconstruction. An additional smearing of the jet energies and directions and a shift of the jet energy scale has been applied in the Monte Carlo, on the basis of an extensive comparison of two-jets events in calibration data collected at the Z^0 peak and in the simulation. The resulting variation (0.36%) in the cross-section has been assigned as a systematic error.
- The sensitivity of the analysis to the jet multiplicity in the event. The results of a modified analysis, where each event has been forced to contain exactly two jets in addition to the isolated photon, have been compared with those from the standard analysis. The difference has been assigned as a systematic error (0.69%).
- The uncertainty related to the models used to simulate the hadronisation process. This uncertainty (0.08%) has been evaluated comparing the results when either the JETSET or the HERWIG hadronisation schemes have been used in the Monte Carlo.
- The uncertainty (0.61%) due to the background subtraction; this is dominated by the 100% uncertainty on the normalisation of the background from two-photon interactions as predicted by HERWIG, which is expected to give the best description of two-photon interactions in the data, and by PYTHIA. This large uncertainty is assigned to cover possible mismodelling of the hard-fragmentation processes in the very small fraction of the two-photon cross-section retained in the selection, as suggested by a comparison with the F2GEN [36] generator. Finally, the uncertainty related to the contamination from fake ISR photons in non-radiative $q\bar{q}$ events is estimated to be 0.35%.

Systematics specific to the $\nu\bar{\nu}\gamma$ channel:

- The uncertainty on the selection efficiency. Systematic errors come from the estimate of the detector occupancy (1%) and from the imperfect description of the conversion probability and of the conversion tagging efficiency in the Monte Carlo (0.8%). A 0.9% uncertainty is assigned to account for systematic effects in the simulation of the cuts used to reject radiative Bhabha and $e^+e^- \rightarrow \gamma\gamma$ events. The uncertainty on the efficiency of the timing cuts used to reject background from cosmic rays translates into a systematic error of 0.5%, while an uncertainty of 0.6% is assigned to cover possible mismodelling of the other cuts complementing the timing requirements in the cosmic and instrumental background rejection. The overall uncertainty on the modelling of the selection efficiency is estimated to be 1.7%. Finally, the statistical uncertainty on the efficiency and feedthrough as estimated from Monte Carlo contributes with a 0.3% uncertainty on the cross-section.
- The uncertainty on the background from processes other than $\nu\bar{\nu}\gamma$, amounting to 0.25%. This includes a 50% systematic uncertainty on the expected background, which was assigned to cover possible mismodelling of the vetoes used in the rejection.

Systematic uncertainties common to both analyses:

- The uncertainty on the angular acceptance arising from residual biases in the coordinate reconstruction and from the absolute knowledge of the detector geometry. The overall uncertainty on the position of the electromagnetic showers, estimated in [37] to be 0.001 rad, results in a relative uncertainty of 0.19%.
- The effects of mismodelling of the energy scale and the resolution of the electromagnetic calorimeter. They have been investigated using a control sample of about one thousand strongly collinear

$e^+e^- \rightarrow \gamma\gamma$ events, whose energies are expected to be very close to the beam energy. The Monte Carlo has been found to reproduce the electromagnetic calorimeter energy scale and resolution in the data within respectively 0.3% and 10%. These differences are in very good agreement with those observed using as a reference process a sample of wide angle Bhabha events [37]. The systematic error has then been estimated by modifying the absolute energy scale and resolution in the Monte Carlo within these limits and the corresponding variation of the cross-section has been taken as systematic error.

- The uncertainty on the beam energy (± 20 MeV). The effect on the cross-section was evaluated by appropriately scaling the energy of the most energetic photon in the Monte Carlo, while leaving unchanged the invariant mass of the system recoiling against the photon.
- The uncertainty on the measurement of the integrated luminosity, 0.22%.

4 Data Interpretation

Since the data presented in the previous section show no evidence of deviations with respect to the Standard Model expectation, they are used to derive bounds on the strength of anomalous $Z\gamma Z$ and $Z\gamma\gamma$ couplings.

4.1 Analysis Procedure

The analysis is based on a comparison of the measured event rate and of the differential distributions with the theoretical predictions for the Standard Model processes and possible contributions from NTGC. The energy spectrum and the cosine of the polar angle of the photon are used in both channels, while in the $q\bar{q}\gamma$ channel the cosine of the angle between the photon and the closest jet is also used. Due to the almost monochromatic photon energy spectrum, this angle is strongly correlated to the quark emission angle in the Z decay rest frame, which is sensitive to NTGC.

The theoretical predictions as a function of different values of the anomalous couplings $h_i^{Z,\gamma}$ are obtained from a Monte Carlo generator [30] for $f\bar{f}\gamma$ production in e^+e^- collisions. This generator is based on the full matrix element, in the lowest order approximation, for all the relevant Standard Model processes and for processes generated by anomalous trilinear neutral gauge couplings. The only Standard Model contribution missing in the calculation is the t-channel W boson exchange in the $\nu\bar{\nu}\gamma$ channel, which has been estimated from NUNUGPV98 and included in the reweighting procedure described in the following. The effect of higher order QED corrections from initial state radiation, which have been found to reduce the contribution from anomalous couplings by typically 15%, has been incorporated into the calculation using a collinear radiator function from the EXCALIBUR [38] Monte Carlo.

The events selected in the data have been classified in $5 \times 4 \times 4$ unequal bins of the three-dimensional $(E_\gamma, \cos \theta_\gamma, \cos \alpha_{\gamma\text{-jet}})$ space. In the case of the $\nu\bar{\nu}\gamma$ channel, the angle between the photon and the Z decay products is not experimentally accessible and therefore integrated out. The NTGC-dependent theoretical prediction for the population in each cell, provided by the Monte Carlo calculation, has been modified to allow for the reconstruction efficiency and resolution effects, as determined from a large sample of fully simulated $Z^0/\gamma \rightarrow q\bar{q}$ and $Z^0 \rightarrow \nu\bar{\nu}$ Standard Model Monte Carlo events. The total number of expected events and the population of each cell as a function of the anomalous

couplings, $N(h_i)$, is determined by reweighting the number N_{SM} of accepted events predicted by the fully simulated Standard Model Monte Carlo according to:

$$N(h_i) = N_{\text{SM}}(1 + \delta(h_i)), \quad \delta(h_i) = \frac{N_{\text{rec}}(h_i) - N_{\text{rec}}(h_i = 0)}{N_{\text{rec}}(h_i = 0)}, \quad (1)$$

where N_{rec} is the number of reconstructed events from the NTGC-dependent theoretical prediction, modified for efficiency and resolution as explained above. Figures 4 and 5 show how the distributions of the kinematic variables, folded with detector effects, are modified by a particular choice of anomalous couplings in the $q\bar{q}\gamma$ and $\nu\bar{\nu}\gamma$ channels. In order to disentangle the effect of NTGC on the event rate and on the differential distributions the latter have been normalised to the number of events selected in the data.

The theoretical expectations for the event rate and the differential distributions have been fitted to the data independently for the two channels, under the hypothesis that only one coupling at a time is non-zero. The most probable values of the anomalous couplings are determined by minimising the negative log-likelihood defined as follows:

$$-\text{LogL} = -\text{LogP}(N^{\text{obs}}, N(h)) - \sum_j \text{LogP}(N_j^{\text{obs}}, N_j(h))$$

where $P(N^{\text{obs}}, N(h))$ is the Poisson probability of observing the number of events N^{obs} if the expectation is $N(h)$. The index j runs over the number of cells defining the multidimensional distributions and the condition $\sum_j N_j(h) = N^{\text{obs}}$ is imposed to disentangle the contributions to the likelihood from event rate and distributions.

The fit procedure has been tested on Monte Carlo samples of Standard Model $q\bar{q}\gamma$ and $\nu\bar{\nu}\gamma$ events reweighted for NTGC effects. The central values of the fit results have been found to correctly reproduce the values of the input NTGC parameters. In order to check the reliability of the errors on the fit results, tests have been performed on several Standard Model Monte Carlo samples of size corresponding to the data luminosity. The distributions of the central values of the couplings determined by the fit are found to be consistent with those expected from the statistical sensitivity.

4.2 Results on Trilinear Neutral Gauge Couplings

The values of the anomalous couplings and the statistical errors obtained from the likelihood fit of the $q\bar{q}\gamma$ and $\nu\bar{\nu}\gamma$ event rate and distributions are listed in table 5, together with the expected statistical sensitivity of the analysis which would be achieved in the case of perfect agreement between data and the Standard Model predictions. In general, the total event rate and the differential distributions have similar sensitivities to NTGC. However, due to the quadratic dependence of the cross-section on the couplings, the fit of the event rate can only determine the value of the couplings with a two-fold ambiguity. In the case of the CP violating couplings, $h_i^{Z,\gamma}$ ($i = 1, 2$), which lead to amplitudes that do not interfere with the Standard Model amplitudes, the sign of the couplings is completely undefined, but both the cross-section and the distributions provide a determination of the absolute value of the couplings. In the case of the CP conserving couplings, $h_i^{Z,\gamma}$ ($i = 3, 4$), the interference with the Standard Model amplitudes results in distributions of the kinematic variables which produce a unique minimum in the associated $-\log L$ function, thus removing the two-fold ambiguity arising from the event rate information.

The 95% Confidence Level (C.L.) bounds on the eight anomalous couplings have been obtained by convolving the likelihood function with a Gaussian whose width σ corresponds to the systematic

uncertainty on the individual parameters, as estimated in section 4.3. The central values and the 95% C.L. intervals resulting from the combination of the two channels are given in table 6. Figures 6 and 7 show the corresponding negative log-likelihood curves for the individual channels and their combination. In combining the results, the correlations between the systematic uncertainties have been taken into account.

4.3 Systematic Errors

The impact of several sources of systematic uncertainty on the NTGC determination has been assessed. Most of the effects considered have already been discussed in the context of the systematic error on the cross-section measurements. A few more are related to the modelling of NTGC effects on the observables used in the likelihood fit and to the reference Standard Model predictions. For all the sources of systematic uncertainty, a symmetric error is assigned based on the maximum absolute shift between the central value, the lower and the upper edges of the 68% C.L. interval as obtained in the standard analysis (table 5) and in a specific fit to the data performed to simulate the systematic effect. The dominant sources of systematic uncertainty come from:

- The effects of the modelling of the selection efficiency. These have been evaluated using the same methods as discussed in section 3.4, and have been assigned as scale uncertainties on the expected number of events in each channel. Where relevant, the angular dependence of the uncertainties has been taken into account. For the $q\bar{q}\gamma$ channel, this includes also the uncertainties coming from the jet multiplicity, the hadronisation modelling and the jet parameter smearing.
- The theoretical uncertainty on the Standard Model prediction. Considerations about missing higher order corrections in the KK2f Monte Carlo lead to an estimate of the theoretical uncertainty of the order of 1% in the $q\bar{q}\gamma$ channel [16]. In the $\nu\bar{\nu}\gamma$ channel, a 2% theoretical uncertainty has been assigned; this uncertainty covers the observed differences between the kinematic cross-sections and the selection efficiencies estimated by KORALZ and NUNUGPV98, and is consistent with a recent comparison between different theoretical calculations presented in [39]. These theoretical uncertainties have been assigned as an overall normalisation error on the Standard Model prediction in each channel.

Other minor contributions to the systematic error have been considered:

- The contribution of the background to the fit result. This has been separated into a component due to a scale factor (corresponding to the Monte Carlo statistical uncertainty on the background absolute rate) and a component due to the modelling of the background shape. The error due to the background normalisation is evaluated as the maximum effect observed when increasing or decreasing the total background rate by one standard deviation. The error due to the shape modelling has been conservatively assessed by assuming a flat distribution of the background events in the signal acceptance region. In the $\nu\bar{\nu}\gamma$ channel, due to the very small contamination, only the uncertainty on the background rate has been considered.
- The uncertainty related to the Monte Carlo statistics. This effect has been estimated by applying the likelihood fit to the data using, as Standard Model prediction in each bin, a number of events generated according to a Poisson distribution with average equal to the prediction of the reference Monte Carlo sample and rescaled to the integrated luminosity of the data. The maximum among the r.m.s of the central values and of the lower and upper 68% C.L. limits on each coupling, over a thousand fits, has been assigned as systematic error.

- The uncertainty on the reweighting procedure coming from the limited Monte Carlo statistics used to evaluate the corrections for resolution and selection efficiency, and from the limited Monte Carlo statistics used in the calculation of the generator-level weights.
- The uncertainty on the missing t-channel W exchange contribution, which applies only to the $\nu\bar{\nu}\gamma$ channel. The procedure used to correct for the missing W t-channel in the reweighting procedure accounts for this process only in the pure Standard Model contribution, but not in the interference between the Standard Model process and the process leading to anomalous coupling. Since the W t-channel is calculated to contribute less than 4% to the Standard Model cross-section in the signal acceptance, the effect of it being neglected in the interference is expected to be of order 2%. The interference term has been conservatively varied by $\pm 4\%$ and the differences in the fit results have been assigned as a systematic error.
- The systematic errors arising from the calorimeter energy scale and resolution, the modelling of the θ_γ angular cut, the uncertainty on the beam energy and on the integrated luminosity. They have been evaluated with the same method as discussed in section 3.4 and have been treated as fully correlated between the $q\bar{q}\gamma$ channel and the $\nu\bar{\nu}\gamma$ channel.

The systematic errors on the couplings are summarised in table 7 for both the $q\bar{q}\gamma$ channel and the $\nu\bar{\nu}\gamma$ channel. For all the couplings the total systematic error is small compared to the statistical uncertainty, except for $h_{3,4}^\gamma$, where the size of the systematic error reaches 60% of the statistical error.

5 Conclusions

Using the data collected at $\sqrt{s} = 189$ GeV, the cross-sections and the differential distributions for hadronic events with a high energy isolated photon and for events with an energetic photon and missing energy have been measured to search for possible contributions from anomalous $Z\gamma Z$ and $Z\gamma\gamma$ couplings. Since no significant evidence of deviations with respect to the Standard Model is observed, 95% C.L. limits on the eight trilinear neutral gauge couplings $h_i^{Z,\gamma}$ have been derived. These limits do not yet allow to place significant constraints on specific models of new physics [6] leading to effective anomalous couplings in the neutral sector. Nevertheless, these results and those presented in [12], which are compatible and of equivalent sensitivity, represent the best available investigations in $e^+e^- \rightarrow Z\gamma$ of the neutral gauge boson self-interactions, in the recently revised theoretical framework describing the general $Z\gamma V$ ($V = Z, \gamma$) vertex.

Acknowledgements

The authors wish to thank U. Baur, G.J. Gounaris and F.M. Renard for helpful discussions and clarifications. We particularly wish to thank the SL Division for the efficient operation of the LEP accelerator at all energies and for their continuing close cooperation with our experimental group. We thank our colleagues from CEA, DAPNIA/SPP, CE-Saclay for their efforts over the years on the time-of-flight and trigger systems which we continue to use. In addition to the support staff at our own institutions we are pleased to acknowledge the

Department of Energy, USA,
National Science Foundation, USA,
Particle Physics and Astronomy Research Council, UK,

Natural Sciences and Engineering Research Council, Canada,
 Israel Science Foundation, administered by the Israel Academy of Science and Humanities,
 Minerva Gesellschaft,
 Benoziyo Center for High Energy Physics,
 Japanese Ministry of Education, Science and Culture (the Monbusho) and a grant under the Monbusho
 International Science Research Program,
 Japanese Society for the Promotion of Science (JSPS),
 German Israeli Bi-national Science Foundation (GIF),
 Bundesministerium für Bildung und Forschung, Germany,
 National Research Council of Canada,
 Research Corporation, USA,
 Hungarian Foundation for Scientific Research, OTKA T-029328, T023793 and OTKA F-023259.

References

- [1] L3 Collaboration, M. Acciarri *et al.*, Phys. Lett. **B467** (1999) 171;
 DELPHI Collaboration, P. Abreu *et al.*, Phys. Lett. **B459** (1999) 382;
 ALEPH Collaboration, R. Barate *et al.*, Phys. Lett. **B422** (1998) 369;
 OPAL Collaboration, G. Abbiendi *et al.*, Eur. Phys. J. **C8** (1998) 191.
- [2] CDF Collaboration, F. Abe *et al.*, Phys. Rev. Lett. **78** (1997) 4536;
 D0 Collaboration, B. Abbott *et al.*, Phys. Rev. **D60** (1999) 72002.
- [3] F.M. Renard, Nucl. Phys. **B196** (1982) 93;
 A. Barroso, F. Boudjema, J. Cole and N. Dombey, Z. Phys. **C28** (1985) 149.
- [4] H. Georgi, Nucl. Phys. **B361** (1991) 339.
- [5] G.J. Gounaris and F.M. Renard, Z. Phys. **C59** (1993) 133.
- [6] G.J. Gounaris, J. Layssac and F.M. Renard, Phys. Rev. **D61** (2000) 73013;
 G.J. Gounaris, J. Layssac and F.M. Renard, “New and Standard Physics contributions to anomalous Z and γ self-couplings”, hep-ph/0003143, March 2000.
- [7] K.J.F. Gaemers and G.J. Gounaris, Z. Phys. **C1** (1979) 259.
- [8] K. Hagiwara, R.D. Peccei and D. Zeppenfeld, Nucl. Phys. **B282** (1987) 253.
- [9] M.Kuroda, F.M.Renard and D. Schildknecht, Phys. Lett. **B183** (1987) 366;
 M. Kuroda, J. Maalampi, D. Schildknecht and K. H. Schwarzer, Nucl. Phys. **B284** (1987) 271;
 Phys. Lett. **B190** (1987) 217;
 C. Grosse-Knetter, I. Kuss and D. Schildknecht, Phys. Lett. **B358** (1995) 87.
- [10] L3 Collaboration, M. Acciarri *et al.*, Phys. Lett. **B412** (1997) 201;
 L3 Collaboration, M. Acciarri *et al.*, Phys. Lett. **B436** (1998) 187;
 DELPHI Collaboration, P. Abreu *et al.*, Phys. Lett. **B380** (1996) 471;
 DELPHI Collaboration, P. Abreu *et al.*, Phys. Lett. **B423** (1998) 194.
- [11] CDF Collaboration, F. Abe *et al.*, Phys. Rev. Lett. **74** (1995) 1941;
 D0 Collaboration, S. Abachi *et al.*, Phys. Rev. **D56** (1997) 6742;
 D0 Collaboration, S. Abachi *et al.*, Phys. Rev. Lett. **78** (1997) 3640;
 D0 Collaboration, B. Abbott *et al.*, Phys. Rev. **D57** (1998) 3817.

- [12] L3 Collaboration, M. Acciarri *et al.*, “ Search for Anomalous $ZZ\gamma$ and $Z\gamma\gamma$ couplings in the process $e^+e^- \rightarrow Z\gamma$ at LEP”, CERN-EP-2000-057, April 28, 2000; Submitted to Phys. Lett. **B**.
- [13] OPAL Collab., K. Ahmet *et al.*, Nucl. Instr. Meth. **A305** (1991) 275.
- [14] B.E. Anderson *et al.*, IEEE Trans. Nucl. Sci. **41** (1994) 845.
- [15] M. Arignon *et al.*, Nucl. Instr. Meth. **A313** (1992) 103;
M. Arignon *et al.*, Nucl. Instr. Meth. **A333** (1993) 330.
- [16] S. Jadach, B.F. Ward and Z. Was, Phys. Lett. **B449** (1999) 97;
<http://home.cern.ch/~jadach/KKindex.html>;
S. Jadach, B.F.L. Ward and Z. Was, “The precision Monte Carlo Event Generator KK for two-fermion final states in e^+e^- Collisions”, hep-ph/9912214, Dec 1999; Submitted to Comp. Phys. Comm..
- [17] S. Jadach, B.F.L. Ward and Z. Was, Comp. Phys. Comm. **79** (1994) 503.
- [18] G. Montagna, M. Moretti, O. Nicosini and F. Piccinini, Nucl. Phys. **B541** (1999) 31.
- [19] PYTHIA Ver. 6.125; T. Sjöstrand, Comp. Phys. Comm. **82** (1994) 74.
- [20] OPAL Collab., G. Alexander *et al.*, Z. Phys. **C69** (1996) 543.
- [21] J. Fujimoto *et al.*, Comp. Phys. Comm. **100** (1997) 128.
- [22] R. Engel, J. Ranft, Phys. Rev. **D54** (1996) 4244.
- [23] G. Marchesini *et al.*, Comp. Phys. Comm. **67** (1992) 465.
- [24] S. Jadach, W. Placzek and B.F.L. Ward, Phys. Lett. **B390** (1997) 298.
- [25] D. Karlen, Nucl. Phys. **B289** (1987) 23.
- [26] Program KORALW V1.42, M. Skrzypek *et al.*, Comp. Phys. Comm. **94** (1996) 216;
M. Skrzypek *et al.*, Phys. Lett. **B372** (1996) 289;
S. Jadach *et al.*, Comp. Phys. Comm. **119** (1999) 272.
- [27] J. A. M. Vermaseren, Nucl. Phys. **B229** (1983) 347;
R. Bhattacharya, J. Smith, G. Grammer, Phys. Rev. **D15** (1977) 3267;
J. Smith, J. A. M. Vermaseren and G. Grammer, Phys. Rev. **D15** (1977) 3280.
- [28] F.A. Berends and R. Kleiss, Nucl. Phys. **B186** (1981) 22.
- [29] J. Allison *et al.*, Nucl. Instr. Meth. **A317** (1992) 47.
- [30] The theoretical prediction for NTGC is obtained with a program based on the formalism defined in U. Baur and E.L. Berger, Phys. Rev. **D47** (1993) 4889, and adapted to the convention established in reference [6].
- [31] OPAL Collab., K. Ackerstaff *et al.*, Eur. Phys. J. **C2** (1998) 441.
- [32] OPAL Collab., K. Ackerstaff *et al.*, Eur. Phys. J. **C1** (1998) 31.
- [33] OPAL Collab., K. Ackerstaff *et al.*, Phys. Lett. **B437** (1998) 218.

- [34] N. Brown and W.J. Stirling, Phys. Lett. **B252** (1990) 657;
 S. Bethke, Z. Kunszt, D. Soper and W.J. Stirling, Nucl. Phys. **B370** (1992) 310;
 S. Catani *et al.*, Phys. Lett. **B269** (1991) 432;
 N. Brown and W.J. Stirling, Z. Phys. **C53** (1992) 629.
- [35] OPAL Collab., G. Abbiendi *et al.*, “Photonic Events with Missing Energy in e^+e^- Collisions at $\sqrt{s} = 189$ GeV”, CERN-EP-2000-060; Submitted to Eur. Phys. J..
- [36] A. Buijs, W.G.J. Langeveld, M.H. Lehto and D.J. Miller, Comp. Phys. Comm. **79** (1994) 523.
- [37] OPAL Collab., G. Abbiendi *et al.*, Eur. Phys. J. **C13** (2000) 553
- [38] F.A. Berends, R. Pittau and R. Kleiss, Comp. Phys. Comm. **85** (1995) 437.
- [39] Y. Kurihara *et al.*, “Event generator for the single and double photon emission associated with neutrino pair-production”, hep-ph/9908422, Aug. 1999.

Efficiencies and Feedthrough		
Channel	Efficiency (%)	Feedthrough (%)
$q\bar{q}\gamma$	87.58 ± 0.12	2.21 ± 0.07
$\nu\bar{\nu}\gamma$	81.04 ± 0.22	1.80 ± 0.08

Table 1: The efficiency and the feedthrough for the $q\bar{q}\gamma$ and $\nu\bar{\nu}\gamma$ selections. In the $\nu\bar{\nu}\gamma$ channel, they are the averages of the KORALZ and the NUNUGPV Monte Carlo. The errors are from Monte Carlo statistics.

Selected Events					
Observed	$q\bar{q}\gamma$ SM	Four-Fermion	Two-Photon	$\tau^+\tau^-$	Total expected
1525	1538.7 ± 5.5	24.3 ± 0.9	9.0 ± 1.0	5.2 ± 0.3	1577.2 ± 5.7

Table 2: The number of selected $q\bar{q}\gamma$ events in the data, compared with the Monte Carlo expectations for the signal and for the background, normalised to the data integrated luminosity. The errors are from Monte Carlo statistics.

Selected Events				
Observed	$\nu\bar{\nu}\gamma$ SM	Physics Background	Instrumental Background	Total expected
370	411.6 ± 2.5	0.72 ± 0.83	0.18 ± 0.18	412.5 ± 2.6

Table 3: The number of $\nu\bar{\nu}\gamma$ events selected in data, the expectation from the $\nu\bar{\nu}\gamma$ Standard Model process, from physics processes other than $\nu\bar{\nu}\gamma$, the expected contamination from cosmic rays and beam-related backgrounds and the overall number of expected events in the $\nu\bar{\nu}\gamma$ channel. The uncertainties reflect either the Monte Carlo statistics or the statistics of the control samples used for the instrumental background estimate.

Systematic errors on the cross section			
$q\bar{q}\gamma$ channel	$\Delta\sigma$ (pb)	$\nu\bar{\nu}\gamma$ channel	$\Delta\sigma$ (pb)
Efficiency	0.115	Efficiency	0.045
Jet Modelling and Reconstruction	0.074	-	-
Background	0.066	Background	0.006
θ_γ Cut	0.018	θ_γ Cut	0.005
Energy Scale	0.009	Energy Scale	0.003
Energy Resolution	0.008	Energy Resolution	0.012
Beam Energy	0.003	Beam Energy	0.001
Luminosity	0.020	Luminosity	0.005
Total Systematic Error	0.154	Total Systematic Error	0.048

Table 4: Systematic errors on the measurement of the cross-section for the $q\bar{q}\gamma$ and $\nu\bar{\nu}\gamma$ channels.

NTGC Fit Results and Expected Sensitivity				
	$q\bar{q}\gamma$ channel		$\nu\bar{\nu}\gamma$ channel	
Coupling	Fit Results	Sensitivity	Fit Results	Sensitivity
h_1^Z	0.000 ± 0.122	± 0.26	0.000 ± 0.166	± 0.35
h_2^Z	0.000 ± 0.081	± 0.17	0.000 ± 0.115	± 0.25
h_3^Z	$-0.055^{+0.122}_{-0.126}$	$-0.33, +0.19$	-0.107 ± 0.169	$-0.48, +0.37$
h_4^Z	$0.035^{+0.082}_{-0.081}$	$-0.14, +0.21$	0.067 ± 0.116	$-0.19, +0.25$
h_1^γ	0.000 ± 0.074	± 0.15	0.000 ± 0.100	± 0.21
h_2^γ	0.000 ± 0.049	± 0.10	0.000 ± 0.069	± 0.15
h_3^γ	$-0.061^{+0.035}_{-0.038}$	$-0.033, +0.031$	$-0.163^{+0.087}_{-0.139}$	$-0.068, +0.064$
h_4^γ	$0.049^{+0.031}_{-0.027}$	$-0.023, +0.025$	$0.138^{+0.143}_{-0.076}$	$-0.045, +0.050$

Table 5: Best fit values of the anomalous couplings and the corresponding statistical errors for the $q\bar{q}\gamma$ and $\nu\bar{\nu}\gamma$ channels. The expected statistical errors, obtained under the hypothesis of perfect agreement with the Standard Model expectations, are also shown.

Combined Results on NTGC		
Coupling	Central Value	95% C.L. Interval
h_1^Z	0.000 ± 0.100	$[-0.190, +0.190]$
h_2^Z	0.000 ± 0.068	$[-0.128, +0.128]$
h_3^Z	$-0.074^{+0.102}_{-0.103}$	$[-0.269, +0.119]$
h_4^Z	$0.046^{+0.068}_{-0.068}$	$[-0.084, +0.175]$
h_1^γ	0.000 ± 0.061	$[-0.115, +0.115]$
h_2^γ	0.000 ± 0.041	$[-0.077, +0.077]$
h_3^γ	$-0.080^{+0.039}_{-0.041}$	$[-0.164, -0.006]$
h_4^γ	$0.064^{+0.033}_{-0.030}$	$[+0.007, +0.134]$

Table 6: Central values and 95% Confidence Level intervals for the eight anomalous couplings as determined from the combination of the $q\bar{q}\gamma$ and the $\nu\bar{\nu}\gamma$ channels. Systematic uncertainties have been incorporated in the errors and in the 95% C.L. limits.

Systematic errors on NTGC		
	$q\bar{q}\gamma$ channel	$\nu\bar{\nu}\gamma$ channel
Δh_1^Z	0.015	0.021
Δh_2^Z	0.009	0.015
Δh_3^Z	0.023	0.025
Δh_4^Z	0.013	0.021
Δh_1^γ	0.009	0.012
Δh_2^γ	0.006	0.009
Δh_3^γ	0.021	0.050
Δh_4^γ	0.016	0.044

Table 7: Absolute systematic errors on the NTGC couplings determined in the $q\bar{q}\gamma$ and in the $\nu\bar{\nu}\gamma$ channel.

OPAL 189 GeV

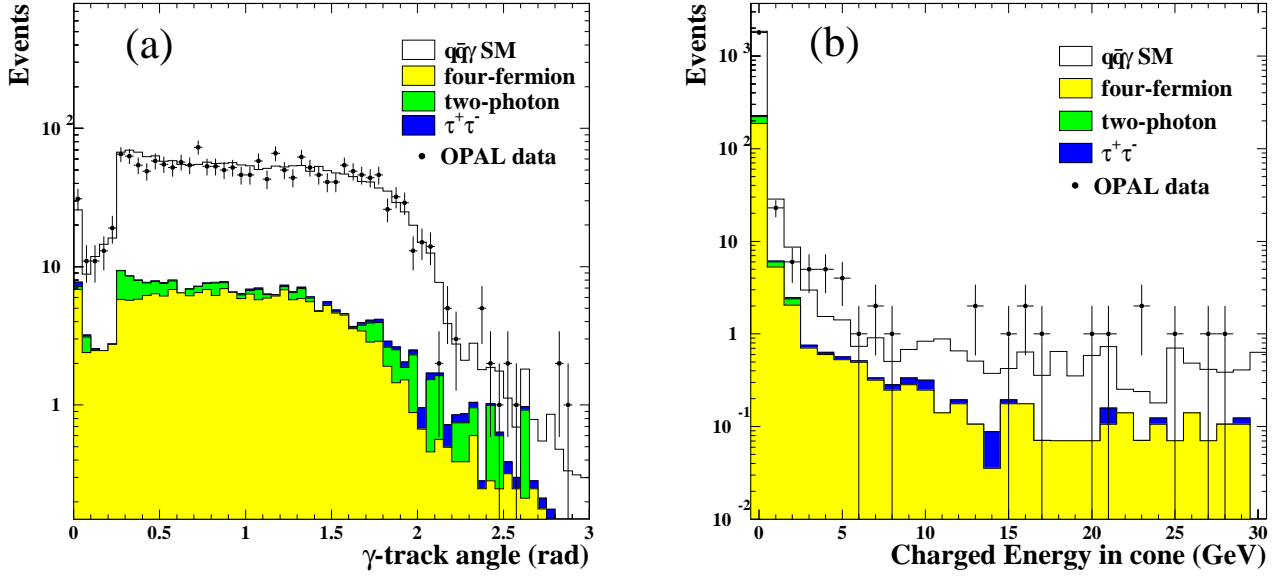


Figure 1: (a) Distribution of the angle between the photon candidate and the closest track; the sharp edge at 0.26 rad reflects the size of the isolation cone. (b) Distribution of the total charged energy in the isolation cone; the explicit cut on this variable is set to 2 GeV. In both cases, the distribution refers to $q\bar{q}\gamma$ events which are accepted or which fail only a single selection criterion. The Monte Carlo prediction is normalised to the integrated luminosity of the data.

OPAL 189 GeV

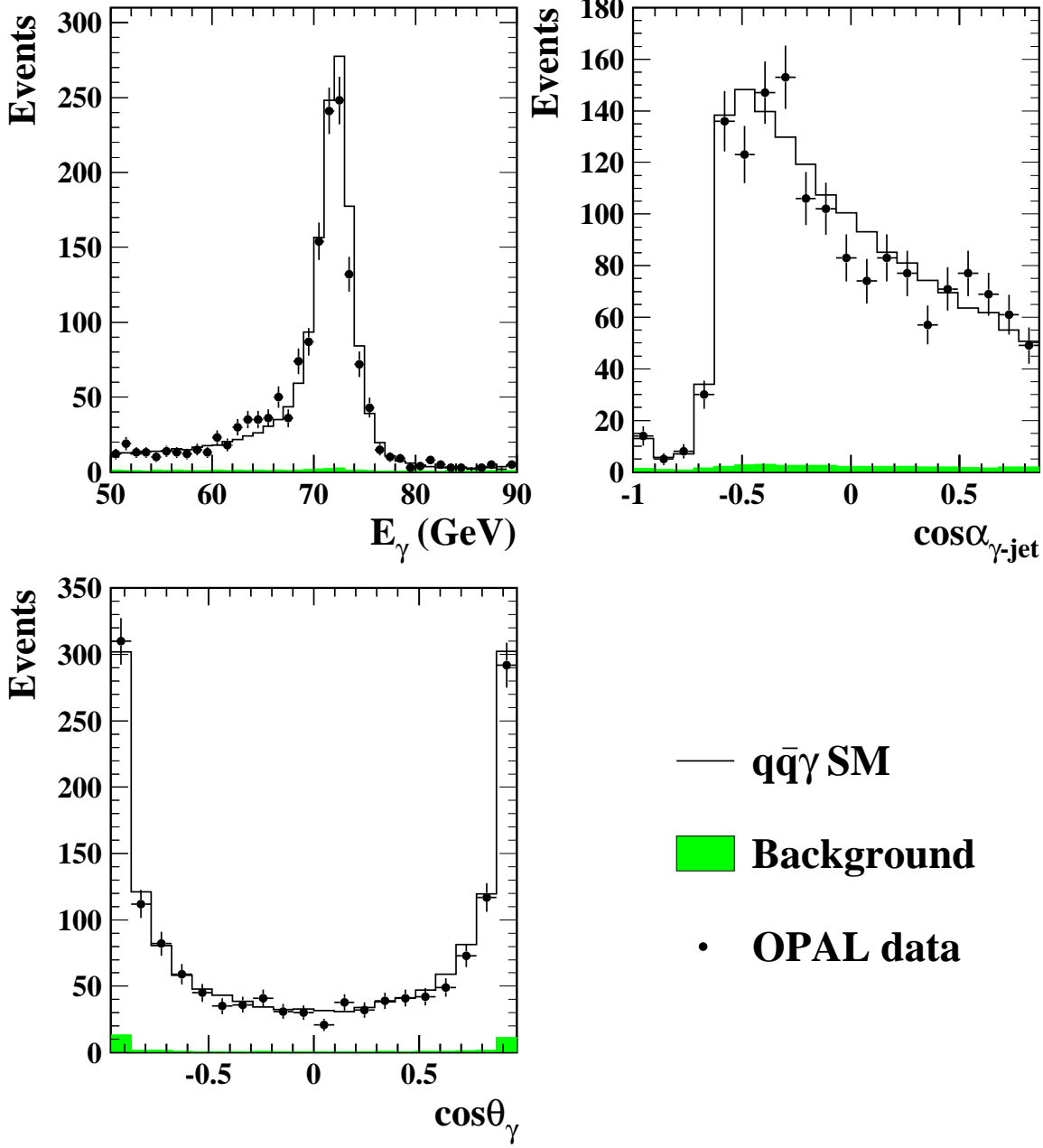


Figure 2: Distribution of E_γ , $\cos\alpha_{\gamma\text{-jet}}$ and $\cos\theta_\gamma$ measured in $q\bar{q}\gamma$ events. The data (dots) are superimposed on the Standard Model predictions from the KK2f Monte Carlo (solid histogram), normalised to the integrated luminosity of the data sample. The shaded area in the histograms represents the background from four-fermion production and two-photon interactions and the contamination from photon candidates not corresponding to truly initial state radiation in $e^+e^- \rightarrow q\bar{q}$ events.

OPAL 189 GeV

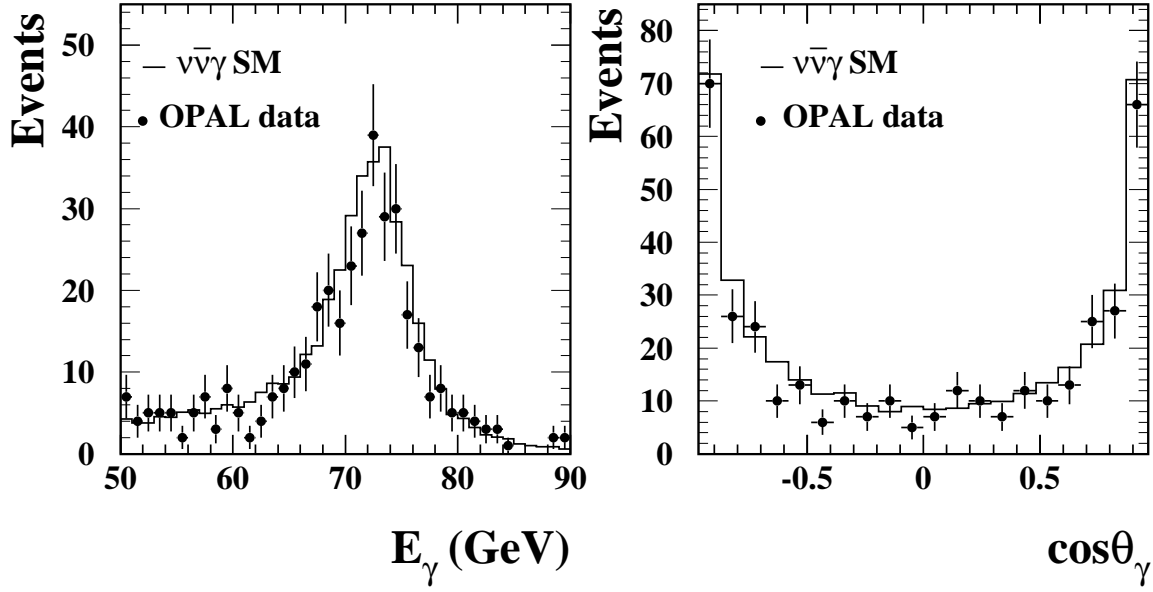


Figure 3: Distribution of kinematic variables E_γ and $\cos\theta_\gamma$ measured in $\nu\bar{\nu}\gamma$ events. The data (dots) are superimposed on the Standard Model prediction (solid histogram), taken as the average of the two generators KORALZ and NUNUGPV98, normalised to the integrated luminosity of the data sample. The negligible ($<0.3\%$) background from physics processes other than $\nu\bar{\nu}\gamma$ is not shown.

OPAL 189 GeV

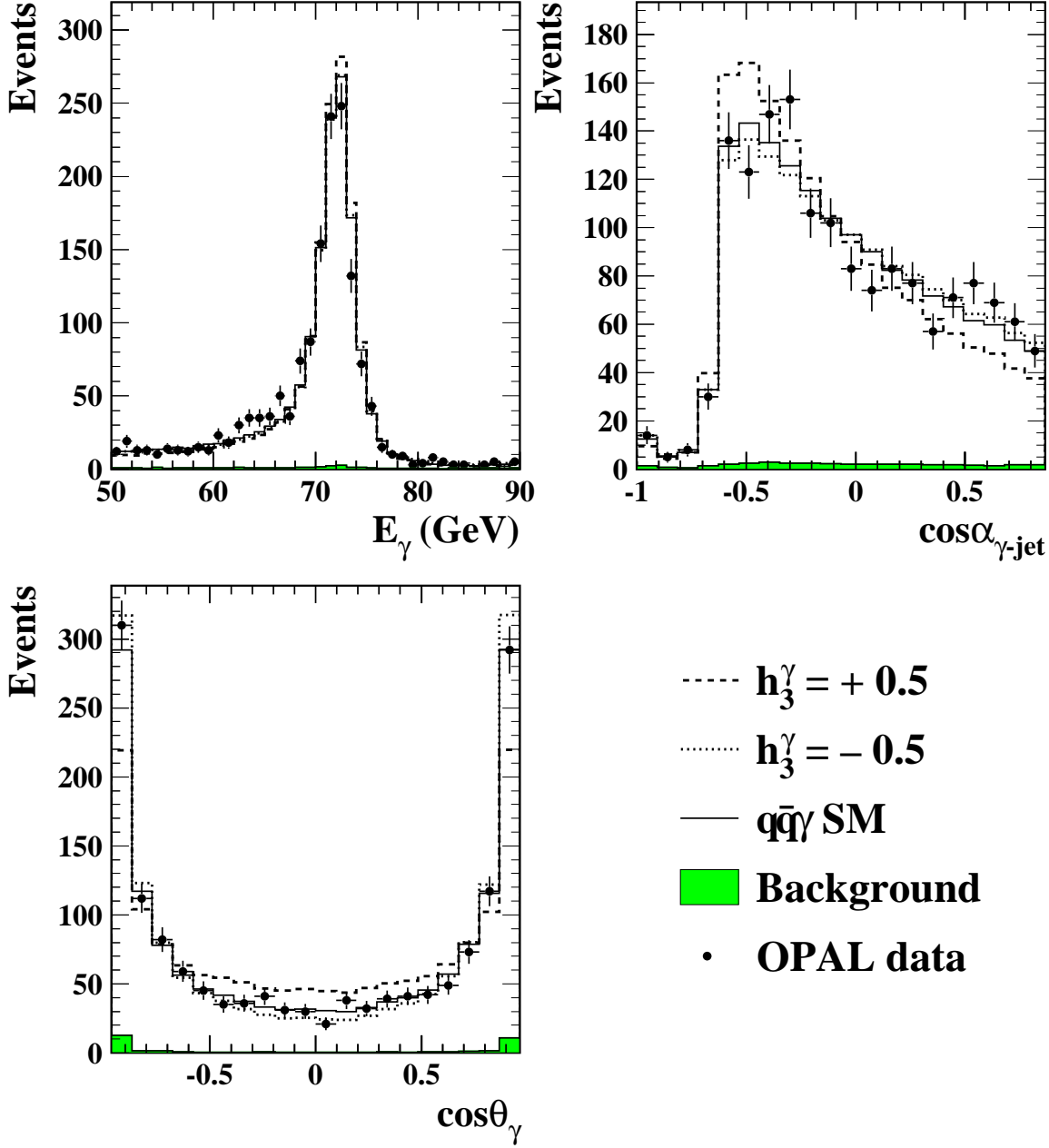


Figure 4: Distribution of kinematic variables E_γ , $\cos\alpha_{\gamma\text{-jet}}$ and $\cos\theta_\gamma$ measured in $q\bar{q}\gamma$ events in the data (dots) and in the KK2f Monte Carlo (solid histogram). The simulated Standard Model expectations, reweighted to incorporate the contributions from $h_3^\gamma = \pm 0.5$ are also shown. The normalisation of the Monte Carlo predictions is defined by the number of events selected in the data.

OPAL 189 GeV

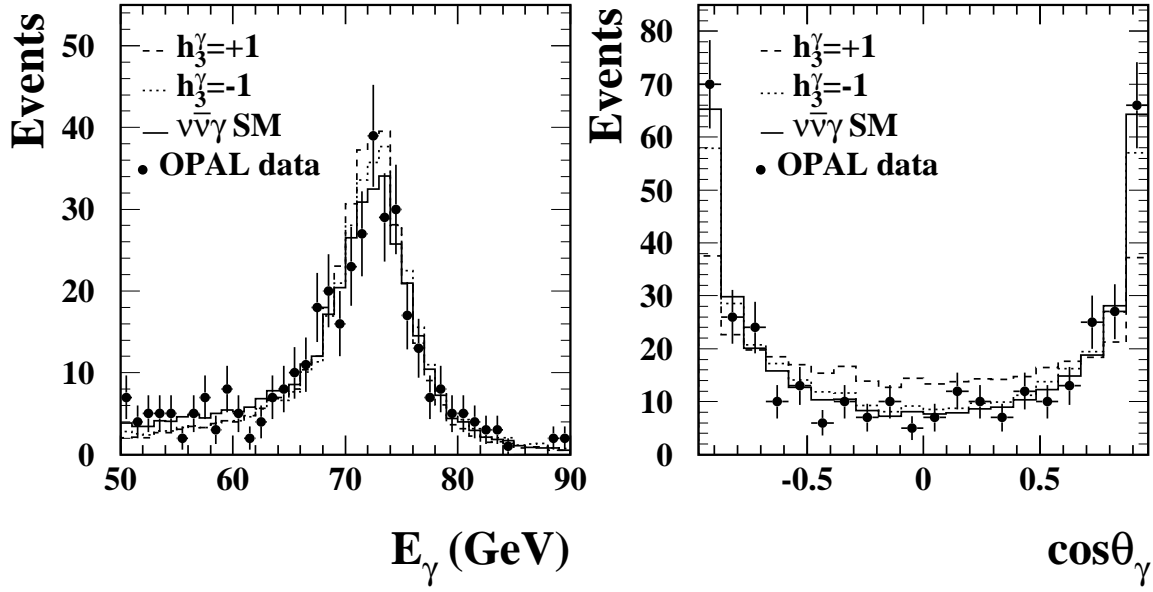


Figure 5: Distribution of kinematic variables E_γ and $\cos\theta_\gamma$ measured in $\nu\bar{\nu}\gamma$ events in the data (dots), and in the Standard Model Monte Carlo (solid line). The simulated Standard Model expectations, reweighted to incorporate the contributions from $h_3^\gamma = \pm 1$ are also shown. The normalisation of the Monte Carlo predictions is defined by the number of events selected in the data.

OPAL 189 GeV

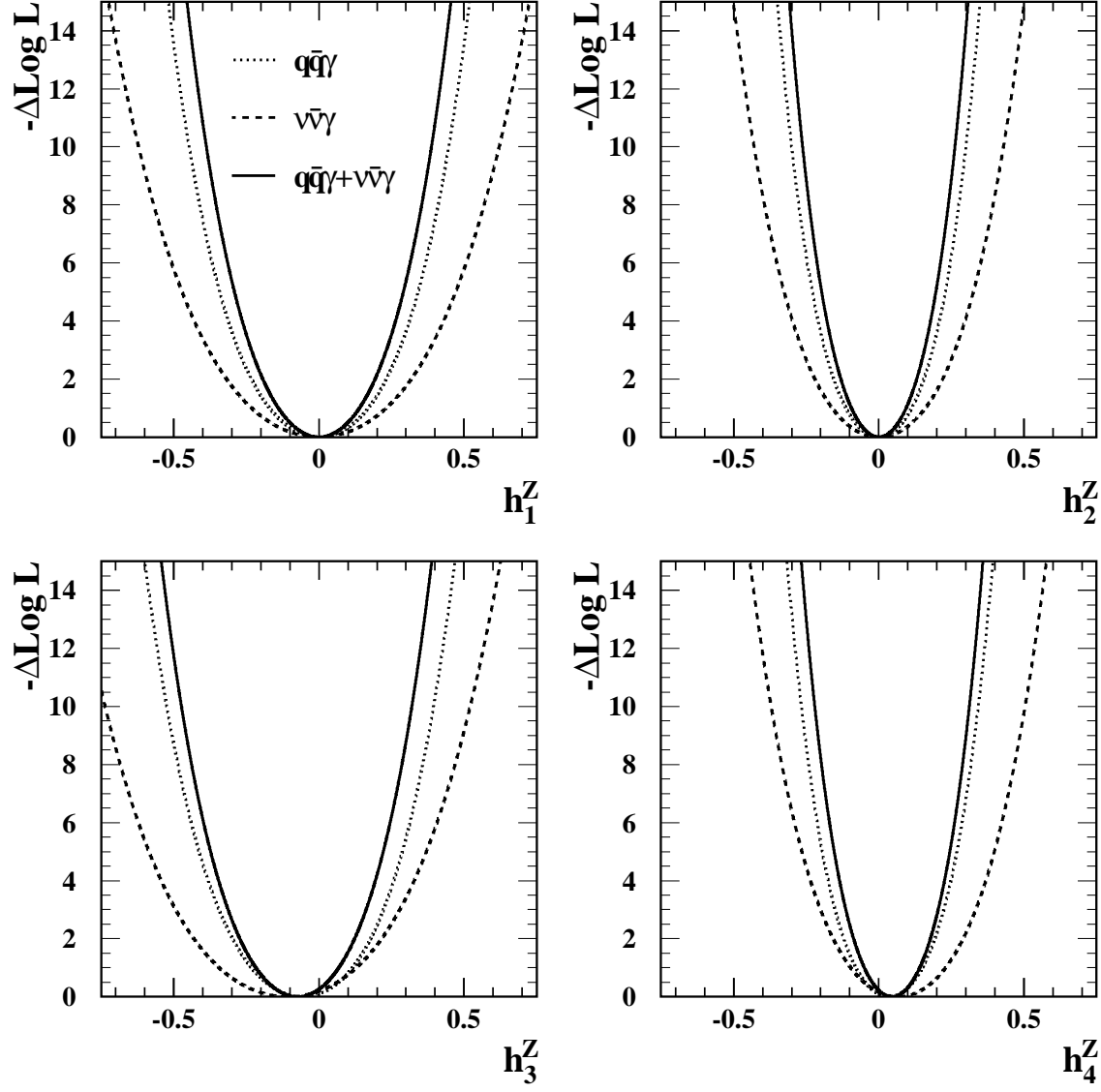


Figure 6: Negative log-likelihood function for the h_i^Z couplings as obtained from the analysis of the $q\bar{q}\gamma$ channel (dash-dotted line), of the $\nu\bar{\nu}\gamma$ channel (dashed line) and from their combination (solid line).

OPAL 189 GeV

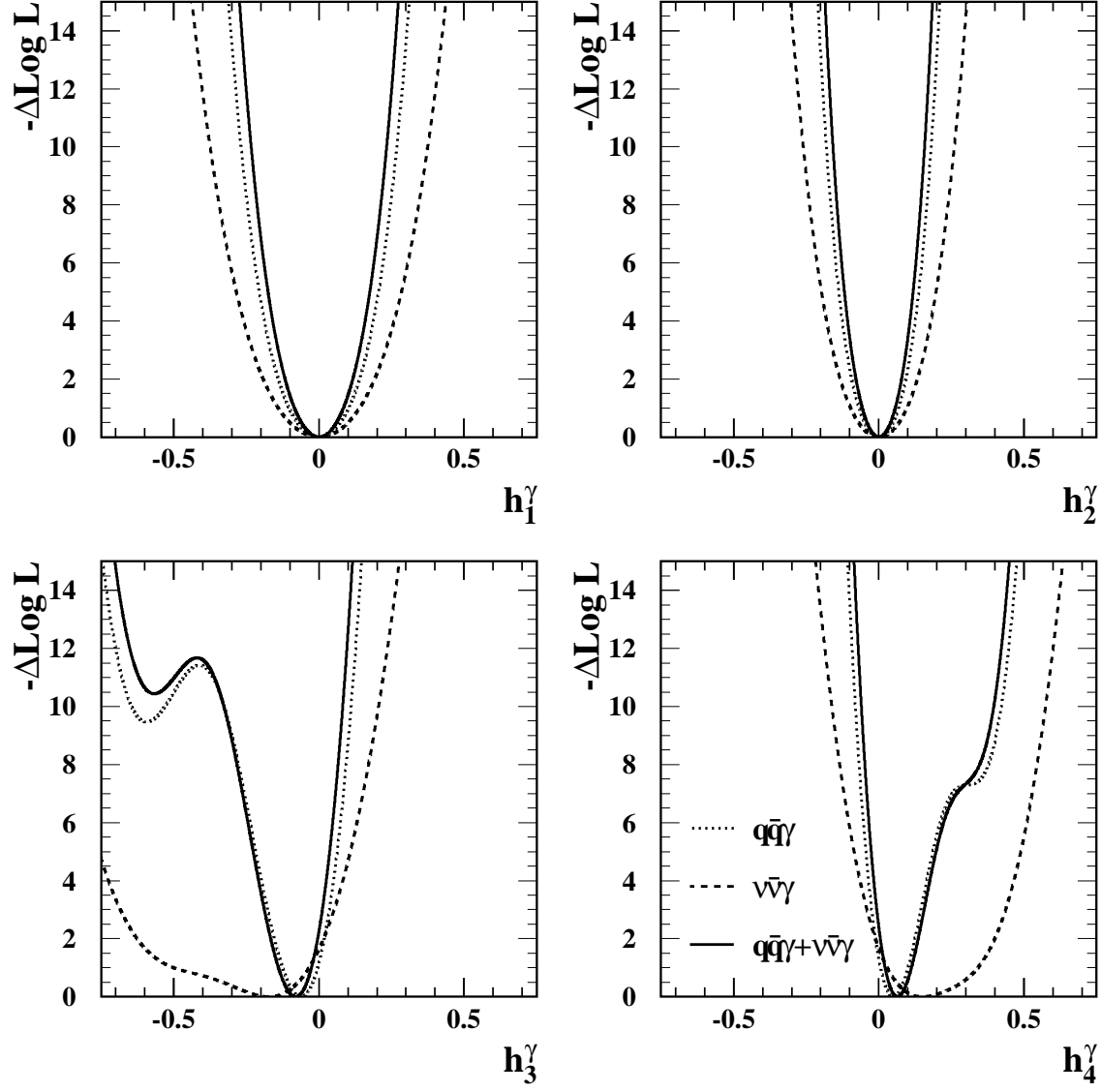


Figure 7: Negative log-likelihood functions for the h_i^γ couplings as obtained from the analysis of the $q\bar{q}\gamma$ channel (dash-dotted line), of the $\nu\bar{\nu}\gamma$ channel (dashed line) and from their combination (solid line).